Magnetic Resonance Imaging 57 (2019) 347–358

Contents lists available at ScienceDirect

Magnetic Resonance Imaging

journal homepage: www.elsevier.com/locate/mri

Original contribution

Incorporating reference guided priors into calibrationless parallel imaging reconstruction

Qingyong Zhu[a], Wei Wang[a,*], Jing Cheng[b], Xi Peng[b]

[a] School of Mathematic & Statistics, Xi'an Jiaotong University, Xi'an 710049, China
[b] Paul C. Lauterbur Research Centre for Biomedical Imaging, Shenzhen Institutes of Advanced Technology, Chinese Academy of Sciences, Shenzhen 518055, China.

ARTICLE INFO

Keywords:
Calibrationless parallel imaging
Joint sparsity
Grey-level intensity
Edge orientation
Multi-scale

ABSTRACT

Purpose: To propose and evaluate a new calibrationless parallel imaging method aimed at further improving the reconstruction accuracy of the accelerated multi-channel MR images.
Method: We introduce a new calibrationless parallel imaging method. On top of exploiting joint sparsity cross channels of the target image to be reconstructed, it incorporates similar priors on the grey-level intensity and edge orientation, which both come from a high-spatial resolution reference image that can be easily obtained in many clinical MRI scenarios. The mixed l_2-l_1 norm is used to enforce joint sparsity and a multi-scale gradient operator is applied to extract fine edges from the reference image. Additionally, this optimization problem can be solved via a non-linear conjugate gradient algorithm with line search in this work.
Results: The proposed method is compared with the existing state-of-the-art auto-calibration and calibrationless parallel imaging techniques. The experiments on different in-vivo brain MR datasets show that the proposed method has the superior performance in terms of both artifact suppression and detail preservation.
Conclusion: The reference guided calibrationless parallel imaging method can significantly improve the performance of joint reconstruction of target channel images. Even when the reduction factor is high, it can keep edge structures well.

1. Introduction

Compressed sensing (CS) [1–3] and parallel imaging (PI) [4–8] are two significant technologies for accelerating the data acquisition in magnetic resonance imaging (MRI). Specifically, the former can help recover the original image without significant information loss from small sampled measurements when the conditions of both image sparsity and incoherent sampling are met. However, the reconstruction quality is highly dependent on the sparsity level of the target image in a certain domain and the returned image usually suffers from severe aliasing artifacts with high reduction factor and noisy measurements. The latter in the two technologies mentioned above can be used to obtain two-fold to four-fold acceleration by exploiting the coil sensitivities or data redundancies across channels, which has been widely used in commercial and clinical MR scanning. However, this method usually causes the amplification of noise and artifact level in reducing encoding.

The combination of CS and PI (CS-PI) has been employed to further reduce sampling requirements and provide improved reconstruction. In this work, the existing CS-PI methods [9–22] can be divided into two categories according to whether the calibration scheme is adopted during the reconstruction.

The calibration approaches [10–15,22] need to estimate the coil sensitivities in advance to help suppress the aliasing artifacts caused by data undersampling. The sensitivity information is usually pre-estimated through fully sampled central k-space data. But it is hard to obtain accurate sensitivity profiles using these limited data, and the biases in pre-estimated sensitivities would bring visible artifacts in final results due to noise and motion. In this group there exist some auto-calibration approaches [9,20,21] that reconstruct both the target image and the corresponding sensitivity. One of the typical examples is the SparseBLIP method [21]. However, this alternate reconstruction based method relies on the initial value, and the returned image suffers from blocky artifacts on account of the total variation regularization.

The calibrationless approaches [16–19,25] encode the sensitivities using the cross-channel correlations to directly reconstruct the multi-channel full k-space or multi-channel images, which can avoid the pre-estimation of sensitivity information. The final image can be obtained as the square root of sum of square (SOS) of the reconstructed multi-channel images. For instance, Shin et al. [16] proposed the SAKE

* Corresponding author at: School of mathematic & statistics, Xi'an an Jiaotong University, Xi'an 710049, China.
E-mail address: wangwei_w@mail.xjtu.edu.cn (W. Wang).

https://doi.org/10.1016/j.mri.2018.12.006
Received 9 May 2018; Received in revised form 27 November 2018; Accepted 19 December 2018

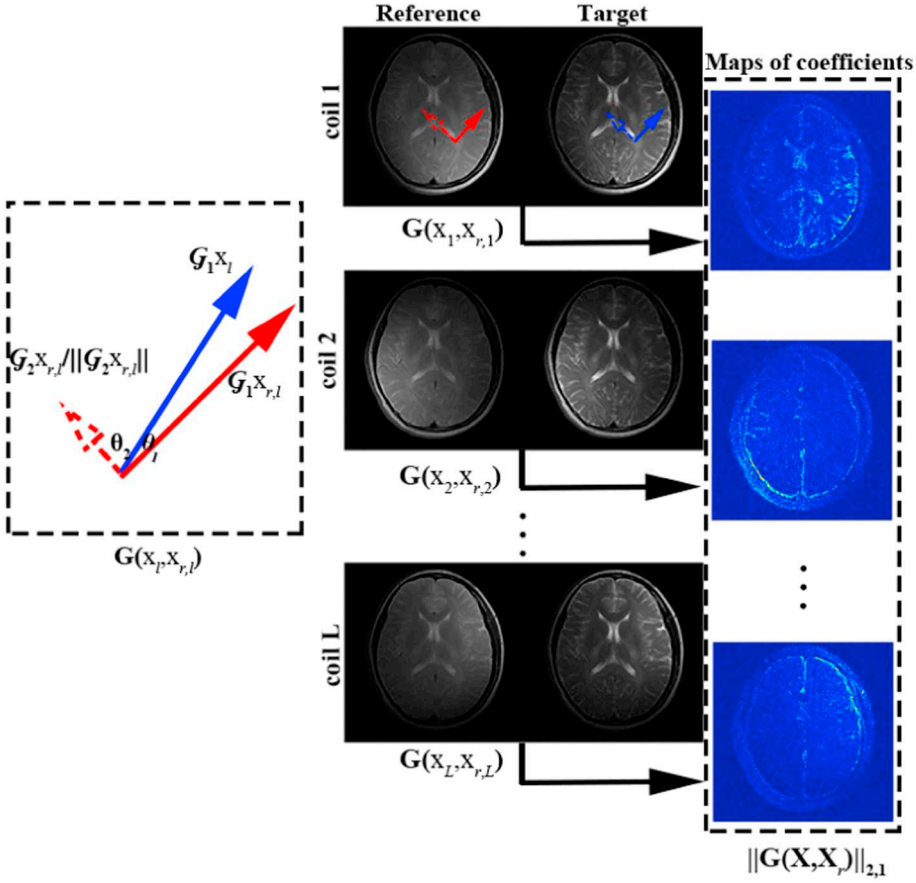

Fig. 1. The reference guided edge orientation regularizing term. The $\mathbf{G}(x_l, x_{r,l})$ represents the projection transform of edge orientation of the target image x_l and reference image $x_{r,l}$. One can use the mixed l_2-l_1 norm to enforce joint sparsity of all channel coefficients in the projection transform domain.

method that estimates and fills the missing multi-channel k-space data by exploiting a structured low-rank matrix completion problem. But estimating the low rank Hankel matrix requires iterative computation of SVD, which is time-consuming and limited in practical applications. Trzasko et al. [17] developed an encouraging reconstruction method called CLEAR to further exploit the low rank property of small patches of k-space and improve the computation efficiency. However, the local cross-channel correlations in the frequency domain do not follow from that in pixel domain [19]. Apart from the above reconstruction methods based on k-space, other methods based on image domain utilize the joint sparsity across channels in a certain transform domain, which have shown an increasing popularity in accelerating calibrationless PI. Among them, one of the earliest works proposed by Mujumdar et al. [18] exploited the spatial correlation between the multi-channel images in wavelet domain via joint sparsity promoting optimization. Chen et al. proposed a FISTA [23,24] based fast joint reconstruction method [25] (we call it FJTV for short), using the cross-channel structural sparsity with total variation as the sparsifying transform. All these methods just formulated calibrationless PI as a joint total variation or joint wavelet regularization task, which fails to provide specific constraints that emphasize the fine edge recovery.

In this paper, we propose a new calibrationless PI method by incorporating reference guided reconstruction priors on the grey-level intensity and edge orientation. The reconstruction model contains three regularizing terms, one of which exploits the joint sparsity of target multi-channel images in finite difference domain, and the other two terms respectively utilize the similarity of intensity variation and gradient orientation between the target image and reference image. The mixed l_2-l_1 norm is adopted to enforce joint sparsity. In addition, we make use of a multi-scale gradient orientation operator to obtain fine edge details in both the strong and weak edge regions of the reference image. The algorithm based on the non-linear conjugate gradient (NLCG) algorithm with line-search [26] is used to solve this optimization problem. The superiority of the proposed method has been demonstrated on different in-vivo brain MR datasets by comparing with state-of-the-art auto-calibration and calibrationless PI methods like SparseBLIP, SAKE and FJTV.

2. Theory & Method

Our proposed approach is demonstrated in the following subsections. We start with the basic PI model and introduce the proposed framework.

2.1. Channel-by-channel CS-PI reconstruction

The k-space data acquisition scheme of PI can be mathematical expressed as:

$$\mathrm{d}_l = \mathbf{F}_u x_l + \mathrm{n}_l, \quad l = 1, 2, \ldots, L \tag{1}$$

where $\mathbf{F}_u \in \mathbb{C}^{M\times N}$ is the under-sampled Fourier encoding matrix with $M \ll N$. $x_l \in \mathbb{C}^{N\times 1}$ and $\mathrm{d}_l \in \mathbb{C}^{M\times 1}$ represent desired image vector with N pixels and k-space measurements with M sampling points for the l-th channel, respectively. n_l denotes the noise vector that is usually assumed to be white complex Gaussian. L is the total number of channels. The CS-PI reconstruction model can be considered as

$$\widehat{x_l} = \arg\min_{x_l} \|\mathbf{F}_u x_l - \mathrm{d}_l\|_2^2 + \lambda \mathbf{\Gamma}(x_l) \tag{2}$$

where $\mathbf{\Gamma}(x_l)$ denotes the regularization term that enforces sparsity of the coefficients in a certain transform domain. The parameter λ is the tradeoff between data consistency and regularization. The final image

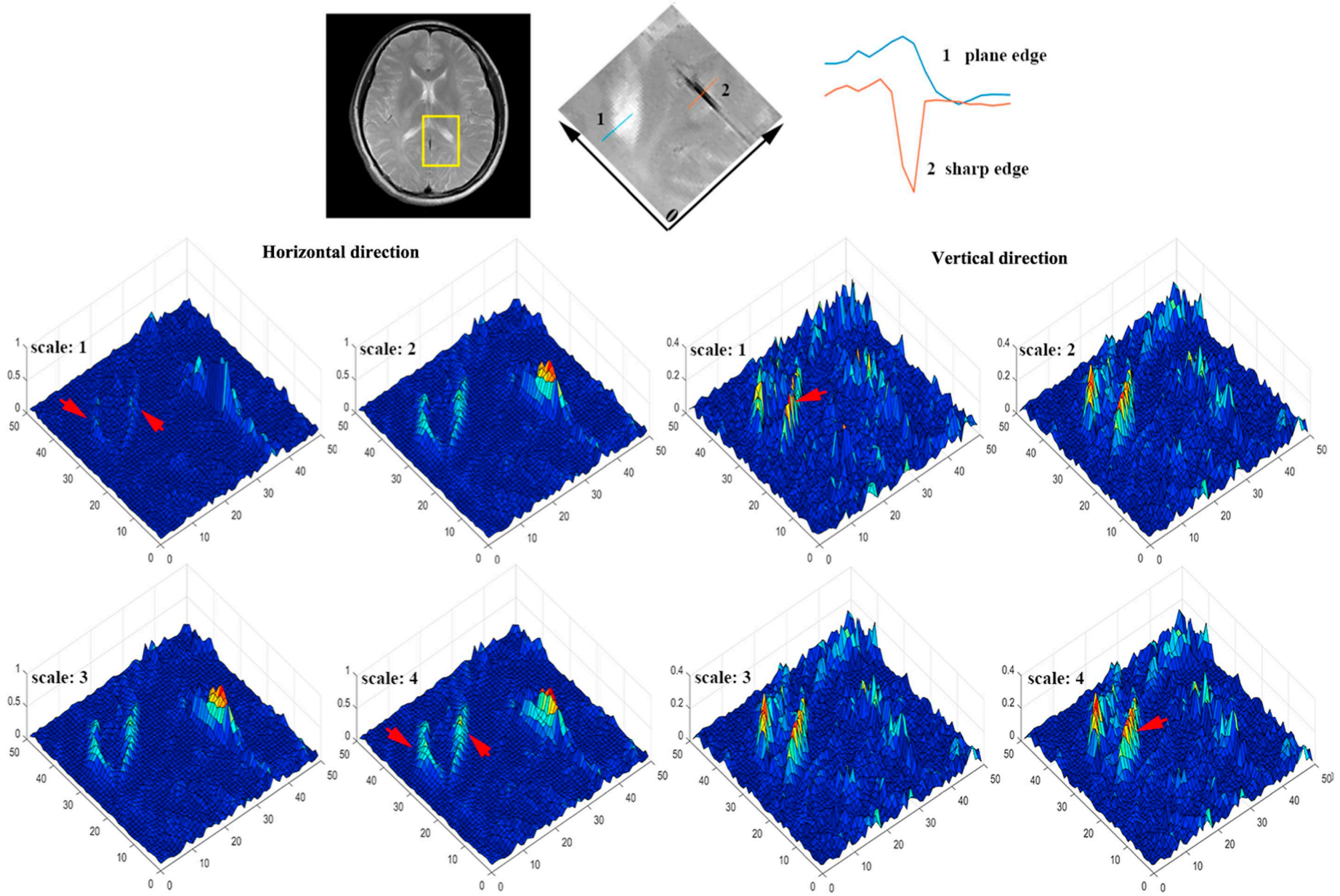

Fig. 2. The edge gradient responses on different scales, i.e., $J = 1, 2, 3$ and 4. Top: one reference image and zoomed-in part of image that contains the weak (blue line) and sharp edges (brown line). Middle-Bottom: the maps of edge gradient responses in horizontal (left) and vertical (right) direction. When J is 4, the information of weak edge can be captured (the red arrows). (For interpretation of the references to colour in this figure legend, the reader is referred to the web version of this article.)

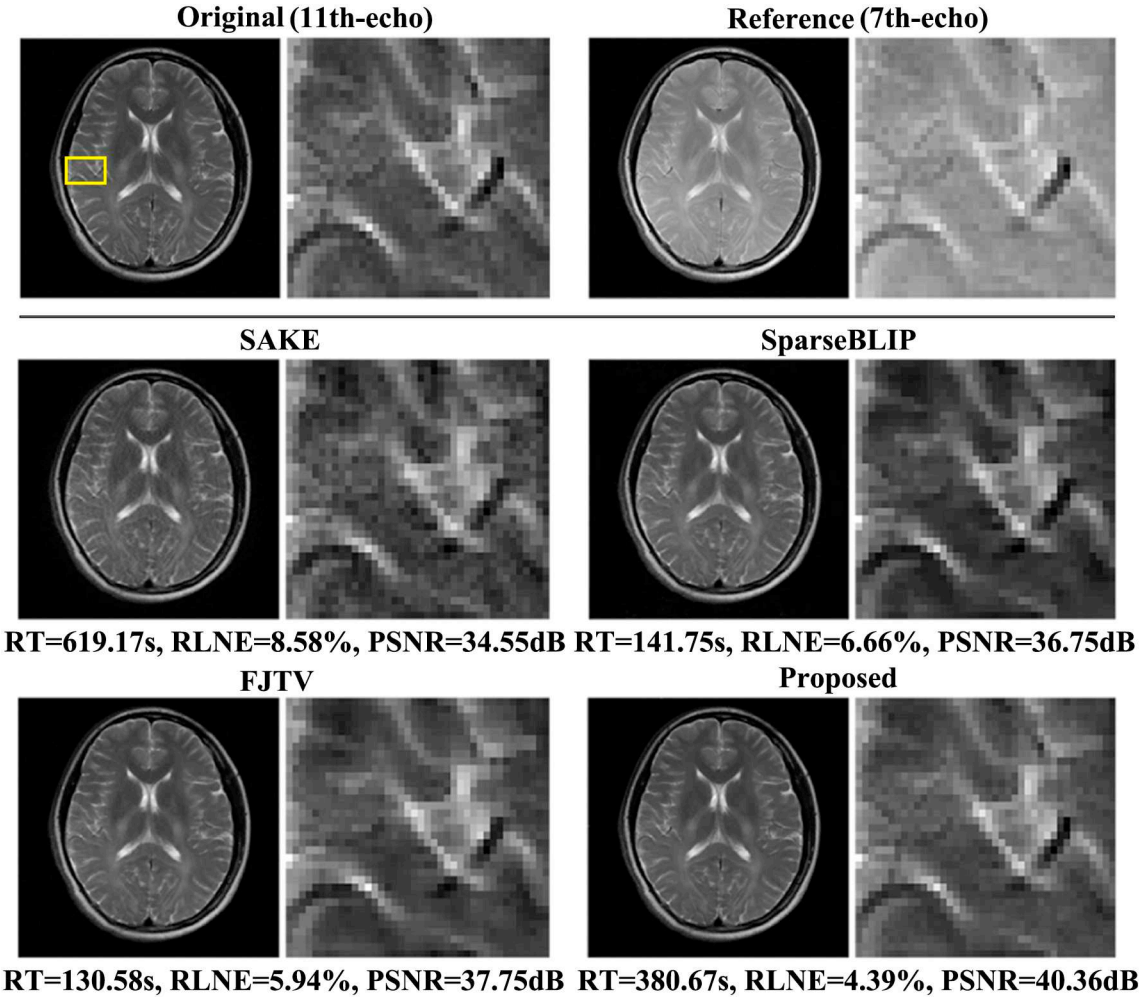

Fig. 3. The reconstruction performance of all methods (SAKE, SparseBLIP, FJTV, and the proposed method) on the in-vivo multi-echo brain images with 1D undersampling mask and reduction factor of 3. The values for the parameters in our proposed method are: $\lambda_1 = 2 \times 10^{-6}$, $\gamma = 4 \times 10^{-3}$, $\lambda_2 = 9 \times 10^{-8}$. The values at the bottom of the reconstructed images are the corresponding RT, RLNE and PSNR values. The part enclosed by the yellow box has been enlarged for better visualization. (For interpretation of the references to colour in this figure legend, the reader is referred to the web version of this article.)

$\widehat{\rho_{sos}}$ is obtained by recombining the reconstructed multi-channel images using the SOS process, i.e., $\widehat{\rho_{sos}} = \sqrt{\sum_{l=1}^{L} \widehat{x_l}^2}$. This method reconstructs separately individual channel image in the standard CS framework [26] and ignores the structured redundancies cross channels leading to a bad performance.

2.2. Calibrationless CS-PI with joint sparsity

These multi-channel images can be reconstructed jointly by solving a classical sparse multiple measurement vectors (MMV) optimization problem (also known as distributed compressed sensing, DCS), which is taken as the following formulation

$$\widehat{\mathbf{X}} = \arg\min_{\mathbf{x}} \left\{ \sum_{l=1}^{L} \|\mathbf{F}_u x_l - \mathrm{d}_l\|_2^2 + \lambda \|\mathbf{\Psi X}\|_{2,1} \right\} \tag{3}$$

where $\mathbf{X} = [x_1, x_2 \dots x_L] \in \mathbb{C}^{N \times L}$ is the image matrix, and each column of $\mathbf{X}$ represents a certain channel image x_l. $\mathbf{\Psi}$ is the sparsifying transform. The mixed l_2-l_1 norm can be defined as $\|\mathbf{\Psi X}\|_{2,1} = \sum_{i=1}^{N} \sqrt{\sum_{l=1}^{L} \|\mathbf{\Psi X}\|_2^2}$, where index i denotes the row and l denotes the column. Since the assumption of the similar sparse mode across channels may be not strictly satisfied, especially in edge regions due to the sensing difference of coil locations, this method fails to obtain higher reconstruction performance than other state-of-the-art auto-calibration or calibrationless methods.

2.3. The proposed joint reconstruction with reference guided priors

In our earlier conference papers [27,28], we have proposed a gradient orientation prior (GOP) to improve the CS based reconstruction. The GOP can be extracted from a high-spatial resolution reference image which usually is obtained by a pre-scan with relative ease. Here we give a PI generalization of earlier works, which is used to improve the calibrationless PI reconstruction and is formulated as,

$$\begin{aligned} \widehat{\mathbf{X}} = \arg\min_{\mathbf{x}} & \sum_{l=1}^{L} \|\mathbf{F}_u x_l - \mathrm{d}_l\|_2^2 \\ & + \lambda_1 \sum_{\alpha=1}^{2} \gamma \, \|\mathbf{D}_\alpha \mathbf{X}\|_{2,1} \\ & + \lambda_1 \sum_{\alpha=1}^{2} (1-\gamma) \|\mathbf{D}_\alpha (\mathbf{X} - \mathbf{X}_r)\|_{2,1} \\ & + \lambda_2 \sum_{\beta=1}^{2} \|\mathbf{G}_\beta (\mathbf{X}, \mathbf{X}_r)\|_{2,1} \end{aligned} \tag{4}$$

where $\mathbf{X}_r = [x_{r,\,1}, x_{r,\,2} \dots x_{r,\,L}] \in \mathbb{C}^{N \times L}$ is the reference image matrix, and each column is a certain channel image $x_{r,\,l}$. All the operators ($\mathbf{D}_\alpha$

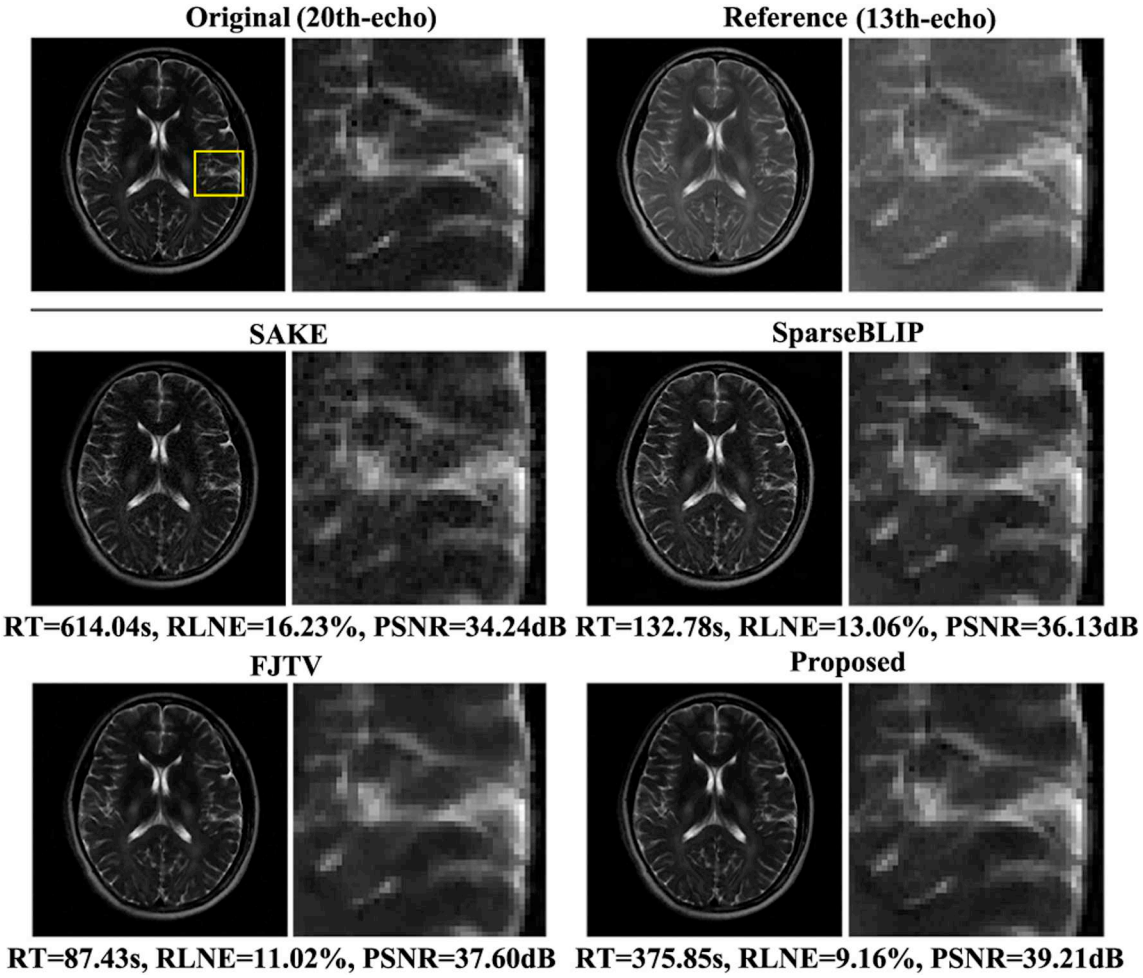

Fig. 4. The reconstruction performance of all methods (SAKE, SparseBLIP, FJTV, and the proposed method) on the in-vivo multi-echo brain images with 2D undersampling mask and reduction factor of 6. The values for the parameters in our proposed method are: $\lambda_1 = 3 \times 10^{-6}$, $\gamma = 3 \times 10^{-3}$, $\lambda_2 = 4 \times 10^{-8}$. The values at the bottom of the reconstructed images are the corresponding RT, RLNE and PSNR values. The part enclosed by the yellow box has been enlarged for better visualization. (For interpretation of the references to colour in this figure legend, the reader is referred to the web version of this article.)

and $\mathbf{D}_\beta$) are conducted in each column of the image matrix. The subscript r denotes the reference. λ_1 and λ_2 are the two parameters that balance the relative importance of the penalties.

The regularizing term of $\sum_{\alpha=1}^{2} \gamma \|\mathbf{D}_\alpha \mathbf{X}\|_{2,1}$ constrains the joint sparsity of the target image coefficients in finite difference domain. $\mathbf{D}_1$ and $\mathbf{D}_2$ denote the finite difference operator in the horizontal and vertical direction. Assuming that one target channel image x_l and the corresponding reference image $x_{r,\,l}$ are similar in most image regions, the difference between them can be modeled as sparse, and hence the mixed l_2-l_1 norm based constraints on all difference images across channels can further improve joint reconstruction. The parameter γ weights the contribution for reference guided intensity prior.

Based on the assumption that the reference image contains the consistent edge orientation information with target image, another regularizing term is proposed by regularizing the edge tangent vector of the target image to be perpendicular to the corresponding edge normal vector in the reference image over all spatial locations. In Fig. 1, we give the demonstration. $\mathscr{G}_1 x_l$ stands for the tangent vectors of the target channel image x_l at spatial locations of edge, $\mathscr{G}_2 x_{r,l}$ represents the normal vectors perpendicular to the corresponding tangent vectors of the reference channel image $x_{r,\,l}$ (e.g., the solid arrow and the dashed arrow). Generally, we have

$$\mathscr{G}_1 x = [\mathcal{M}_1 x, \mathcal{M}_2 x]; \quad \mathscr{G}_2 x = [\mathcal{M}_2 x, -\mathcal{M}_1 x]$$

Since the anatomy of x_l is well aligned with $x_{r,\,l}$, the angle θ_1 between edge orientation at same location should be approximately 0° and angle θ_2 should approach 90°, that is to say, the edge orientation of x_l is orthogonal to the edge normal orientation of $x_{r,\,l}$, we have

$$\begin{aligned}\mathbf{G}(x_l, x_{r,l}) &= \left\langle \mathscr{G}_1 x_l, \frac{\mathscr{G}_2 x_{r,l}}{|\mathscr{G}_2 x_{r,l}|} \right\rangle \\ &= \frac{[\mathcal{M}_1 x_l, \mathcal{M}_2 x_l][\mathcal{M}_2 x_{r,l}, -\mathcal{M}_1 x_{r,l}]^T}{|[\mathcal{M}_2 x_{r,l}, -\mathcal{M}_1 x_{r,l}]|} \\ &= \frac{\mathcal{M}_1 x_l \mathcal{M}_2 x_{r,l} - \mathcal{M}_2 x_l \mathcal{M}_1 x_{r,l}}{|[\mathcal{M}_2 x_{r,l}, -\mathcal{M}_1 x_{r,l}]|} \\ &\approx 0 \end{aligned} \tag{5}$$

here $\langle \cdot, \cdot \rangle$ denotes row vector inner product. We normalized the normal vectors of the reference image to solely preserve directional information. $|\cdot|$ returns a column vector, the elements of which are the l_2 norm of the row vectors of the input argument. Additionally, we controls the strength of the edge orientation regularization by the weight $\frac{1}{\sqrt{|[\mathcal{M}_2 x_{r,l}, -\mathcal{M}_1 x_{r,l}]|}}$ according to the weighting scheme in the work [29,30], and we can change the Expression (5) to

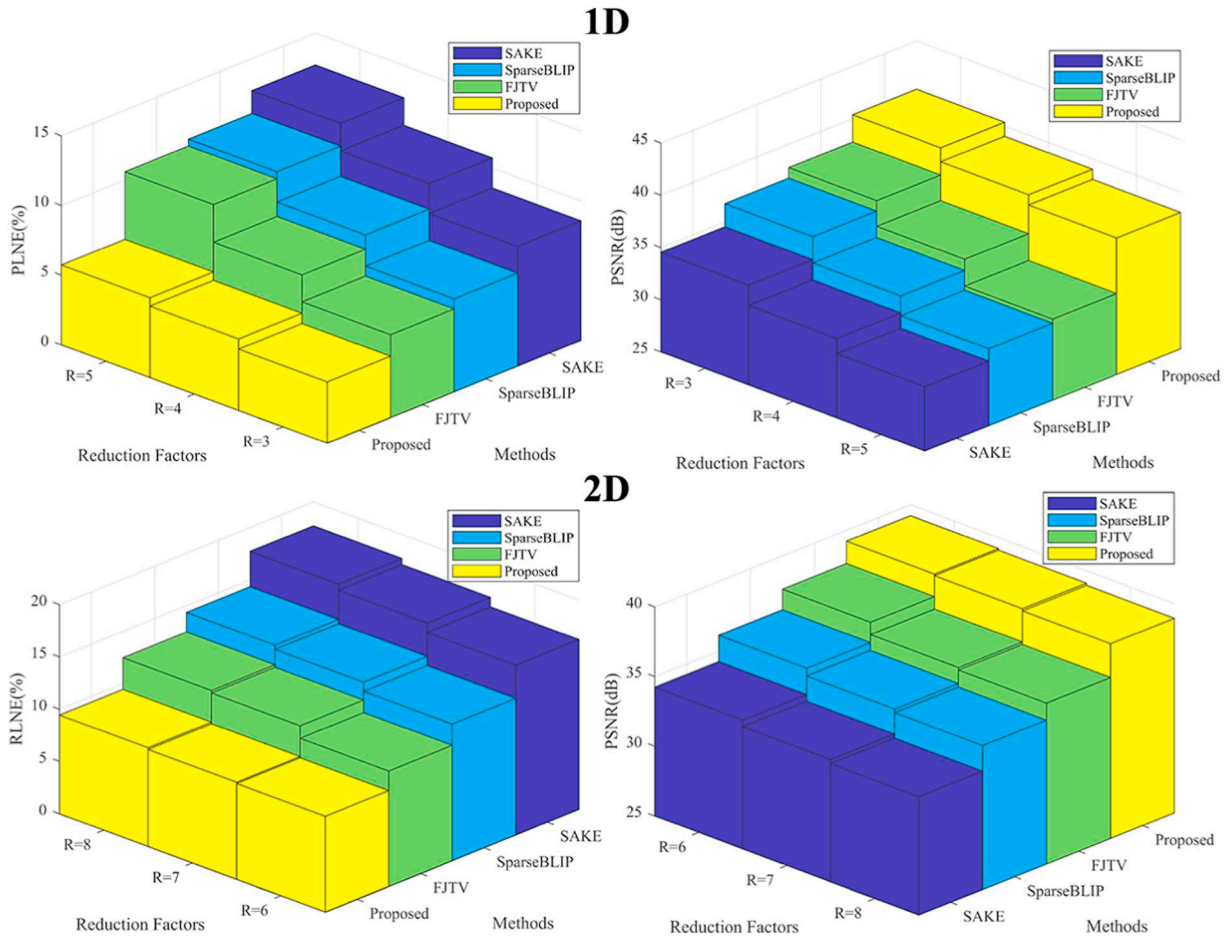

Fig. 5. The histograms of the reconstruction RLNE (left) and PSNR (right) values of in-vivo multi-echo brain images using SAKE, SparseBLIP, FJTV, and the proposed method at various reduction factors (R = 3, 4, 5 for 1D and R = 6, 7, 8 for 2D).

$$\begin{aligned}&\mathbf{G}(x_l, x_{r,l})\\&= \frac{1}{\sqrt{|[\mathcal{M}_2 x_{r,l}, -\mathcal{M}_1 x_{r,l}]|}}\\&\quad \frac{[\mathcal{M}_1 x_l, \mathcal{M}_2 x_l][\mathcal{M}_2 x_{r,l}, -\mathcal{M}_1 x_{r,l}]^T}{|[\mathcal{M}_2 x_{r,l}, -\mathcal{M}_1 x_{r,l}]|}\\&= \frac{1}{\sqrt{|[\mathcal{M}_2 x_{r,l}, -\mathcal{M}_1 x_{r,l}]|}} \frac{\mathcal{M}_1 x_l \mathcal{M}_2 x_{r,l} - \mathcal{M}_2 x_l \mathcal{M}_1 x_{r,l}}{|[\mathcal{M}_2 x_{r,l}, -\mathcal{M}_1 x_{r,l}]|}\end{aligned} \tag{6}$$

where $\mathcal{M}_1 x \in \mathbb{C}^{N\times 1}$ and $\mathcal{M}_2 x \in \mathbb{C}^{N\times 1}$ denote the multi-scale gradients [31] of input image x in first and second coordinate respectively. We have

$$\mathcal{M}_1 x = \begin{cases} vec\left(\frac{1}{J}\sum_{j=1}^{J} \frac{\mathbf{x}(s+j,t) - \mathbf{x}(s,t)}{\sqrt{j}}\right), \beta = 1 \\ vec\left(\frac{1}{J}\sum_{j=1}^{J} \frac{\mathbf{x}(s+j,t+j) - \mathbf{x}(s,t)}{\sqrt{j}}\right), \beta = 2 \end{cases}$$

$$\mathcal{M}_2 x = \begin{cases} vec\left(\frac{1}{J}\sum_{j=1}^{J} \frac{\mathbf{x}(s,t+j) - \mathbf{x}(s,t)}{\sqrt{j}}\right), \beta = 1 \\ vec\left(\frac{1}{J}\sum_{j=1}^{J} \frac{\mathbf{x}(s,t+j) - \mathbf{x}(s+j,t)}{\sqrt{j}}\right), \beta = 2 \end{cases}$$

where J is the scale number and the bold letter $\mathbf{x}$ denotes image matrix. s and t are the row and column indexes of image matrix. Obviously, $\mathbf{G}_1(\mathbf{X}, \mathbf{X}_r)$ and $\mathbf{G}_2(\mathbf{X}, \mathbf{X}_r)$ represents two reference guided edge orientation constraints under different decomposition patterns on edge orientation.

The Fig. 2 shows the gradient responses of both sharp and plane edges at different scales. We can clearly observe that when J is 1, the responses of gradient on plane regions are small, as labelled by the red arrow. This is because when the values of adjacent pixels in weak edges are near, the edge gradient fails to capture the signal change. And when J is 4, the response of gradient on edges is large and the tiny difference of weak edges can be effectively captured. The captured fine priors could further help recover the edge structures that fail to be restored in other methods.

2.4. The gradient computation in NLCG algorithm

To solve the optimization problem in this work, the NLCG algorithm with line search was adopted. The core steps to compute the gradients of the regularizing terms with respect to the desired multi-channel image matrix $\mathbf{X}$ are presented as below:

$$\frac{\partial \|\mathbf{D}_\alpha \mathbf{X}\|_{2,1}}{\partial \mathbf{X}} = \mathbf{D}_\alpha^H \left(\frac{\mathbf{D}_\alpha \mathbf{X}}{|\mathbf{D}_\alpha \mathbf{X}|}\right), \alpha = 1, 2$$

where $\mathbf{D}_\alpha{}^H$ is the adjoint operator of $\mathbf{D}_\alpha$. Similarly, for the gradients of other regularizing terms, we have

$$\frac{\partial \|\mathbf{D}_\alpha (\mathbf{X} - \mathbf{X}_r)\|_{2,1}}{\partial \mathbf{X}} = \mathbf{D}_\alpha^H \left(\frac{\mathbf{D}_\alpha (\mathbf{X} - \mathbf{X}_r)}{|\mathbf{D}_\alpha (\mathbf{X} - \mathbf{X}_r)|}\right), \alpha = 1, 2$$

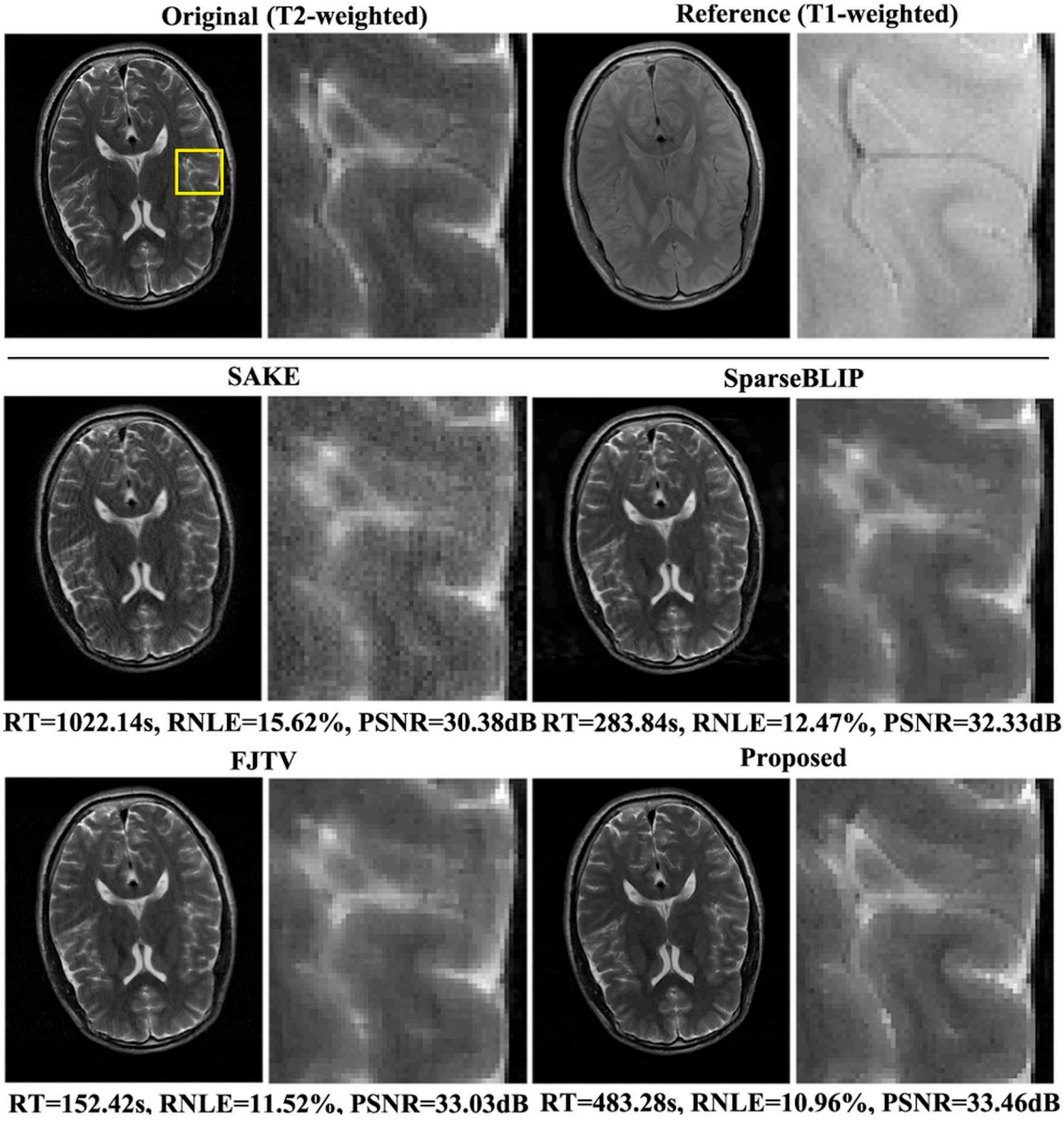

Fig. 6. Reconstruction performance of all methods (SAKE, SparseBLIP, FJTV, and the proposed method) on the in-vivo multi-contrast brain images with 1D undersampling mask and reduction factor of 4. The values for the parameters in our proposed method are: $\lambda_1 = 1.6 \times 10^{-6}$, $\gamma = 5 \times 10^{-1}$, $\lambda_2 = 1 \times 10^{-7}$. The values at the bottom of the reconstructed images are the corresponding RT, RLNE and PSNR values. The part enclosed by the yellow box has been enlarged for better visualization. (For interpretation of the references to colour in this figure legend, the reader is referred to the web version of this article.)

$$\frac{\partial \ \|\mathbf{G}_\beta(\mathbf{X},\mathbf{X}_r)\|_{2,1}}{\partial \mathbf{X}} = \mathbf{G}_\beta^H\left(\frac{\mathbf{G}_\beta(\mathbf{X},\mathbf{X}_r)}{|\mathbf{G}_\beta(\mathbf{X},\mathbf{X}_r)|},\mathbf{X}_r\right),\ \beta = 1,\ 2$$

Here the $\mathbf{D}_\beta{}^H$ is the adjoint operator of $\mathbf{D}_\beta{}^H$ and $\mathbf{D}_\beta{}^H(x, x_{r,\ l})$ is represented as.

following

$$\mathbf{G}_\beta^H(x, x_{r,l}) = \mathcal{M}_1^H\left(\left(\frac{\mathcal{M}_2 x_{r,l}}{|[\mathcal{M}_2 x_{r,l}, -\mathcal{M}_1 x_{r,l}]|}\right)^* \odot x\right) - \mathcal{M}_2^H\left(\left(\frac{\mathcal{M}_1 x_{r,l}}{|[\mathcal{M}_2 x_{r,l}, -\mathcal{M}_1 x_{r,l}]|}\right)^* \odot x\right)$$

where $*$ denotes conjugation and $\odot$ represents the Hadamard product. In the implementation, the $\frac{\mathcal{M}_1 x_{r,l}}{|[\mathcal{M}_2 x_{r,l}, -\mathcal{M}_1 x_{r,l}]|}$ and $\frac{\mathcal{M}_2 x_{r,l}}{|[\mathcal{M}_2 x_{r,l}, -\mathcal{M}_1 x_{r,l}]|}$ can be computed at the beginning of the NLCG algorithm and used repeatedly.

3. Experiments & results

In this section, we demonstrate the effectiveness of the proposed method in three clinical MRI scenarios, all of which use a reference image to improve the reconstruction performance. Undersampled k-space data was retrospectively obtained using two undersampling schemes including 1D and 2D random undersampling with the variable density. The calibrationless methods (SAKE and FJTV) and the auto-calibration method (SparseBLIP) were conducted for comparison. The model parameters in all methods were elaborately tuned to provide the best performance. In the SparseBLIP, we set the calibration size as 32×32. All the algorithms were run for approximately 200 iterations except that the CG based methods including SparseBLIP and the proposed method both ran 8 iterations due to their high computational complexity. All experiments were conducted in Matlab R2017a on a standard laptop (Lenovo E430 with Windows 10 and 64 bit operation system, Intel Corei5-3210 processor, 2.50 GHz, 8 GB RAMS). The

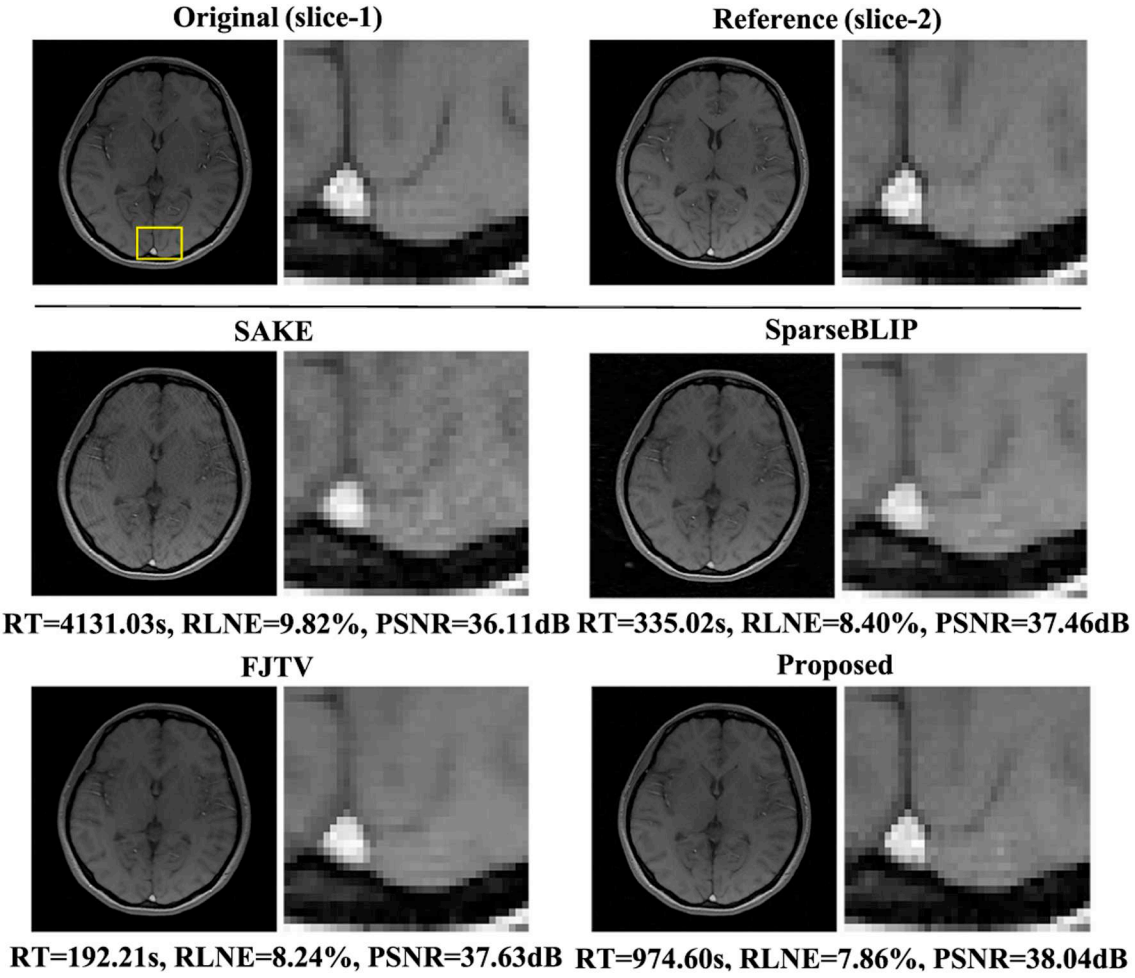

Fig. 7. Reconstruction performance of all methods (SAKE, SparseBLIP, FJTV, and the proposed method) on the in-vivo multi-slice brain images with 1D undersampling mask and reduction factor of 4. The values for the parameters in our proposed method are: $\lambda_1 = 1 \times 10^{-6}$, $\gamma = 5 \times 10^{-1}$, $\lambda_2 = 4 \times 10^{-8}$. The values at the bottom of the reconstructed images are the corresponding RT, RLNE and PSNR values. The part enclosed by the yellow box has been enlarged for better visualization. (For interpretation of the references to colour in this figure legend, the reader is referred to the web version of this article.)

running time (RT) is measured to evaluate the algorithm efficiency. The quality of the reconstructed images can be quantified with the relative l2-norm error (RLNE) and peak signal to noise ratio (PSNR), which are defined as

$$\mathrm{RLNE} = \frac{\|\widehat{\rho_{SOS}} - \rho_{SOS}\|_2}{\|\rho_{SOS}\|_2}, \quad \mathrm{PSNR} = 20\log_{10}\frac{\max(\rho_{SOS})\sqrt{N}}{\|\widehat{\rho_{SOS}} - \rho_{SOS}\|_2}$$

where ρ_{SOS} and $\widehat{\rho_{SOS}}$ denote the SOS-combined fully-sampled original image and the reconstructed image, respectively.

3.1. The experiments on multi-echo brain image dataset

This experiment uses the multi-echo brain MR dataset acquired on a 3.0 T Siemens scanner using a turbo spin echo sequence with a 4-channel head coil array (matrix size = 256 × 256, slice thickness = 3.0 mm, TR = 4000 ms, echo train length = 32, ΔTE = 10 ms). The echo image obtained at an earlier time was regarded as the reference image, and another echo image obtained at the later time was regarded as the target image.

We first tested all methods with 1D undersampling pattern with reduction factor of 3. The reference and target image are from 7th-echo time and 11th-echo time, respectively. The results are shown in the Fig. 3. Specifically, for the SAKE method, obvious artifacts can be observed from the returned image and both of the SparseBLIP and FJTV method can provide better reconstructions than SAKE but suffer from some blurry in edge regions. With the help of the reference guided similar priors, the proposed method has less aliasing and preserves fine edge details across the whole image. Moreover, all methods were evaluated on another slice brain dataset with 2D undersampling pattern at reduction factor of 6 for further comparison. Similar conclusions can be drawn from the reconstruction results in Fig. 4. Observed from the corresponding zoomed-in region, the proposed method produces an image closest to the original image and has clearer edge details than other methods.

In addition, the RLNE and PSNR values of these reconstructed images at various reduction factors (R = 3, 4, 5 for 1D and R = 6, 7, 8 for 2D) were plotted in the form of 3-dimensional histograms. As shown in Fig. 5, the proposed method keeps outperforming the other methods with the lowest RLNE and the highest PSNR values. It can be easily noticed that the quantitative results of the proposed method do not worsened significantly with the increasing reduction factor, showing the high robustness.

3.2. The experiments on multi-contrast and multi-slice brain image datasets

To demonstrate the availability of the proposed method, we added more experiments where the target and reference images are acquired at different contrasts or different anatomical slices.

The multi-contrast image dataset was scanned with a 3 T Siemens scanner using the turbo spin echo sequence with 4-channel head coil array (matrix size = 384 × 324, FOV = 230 × 187 mm^2, slice

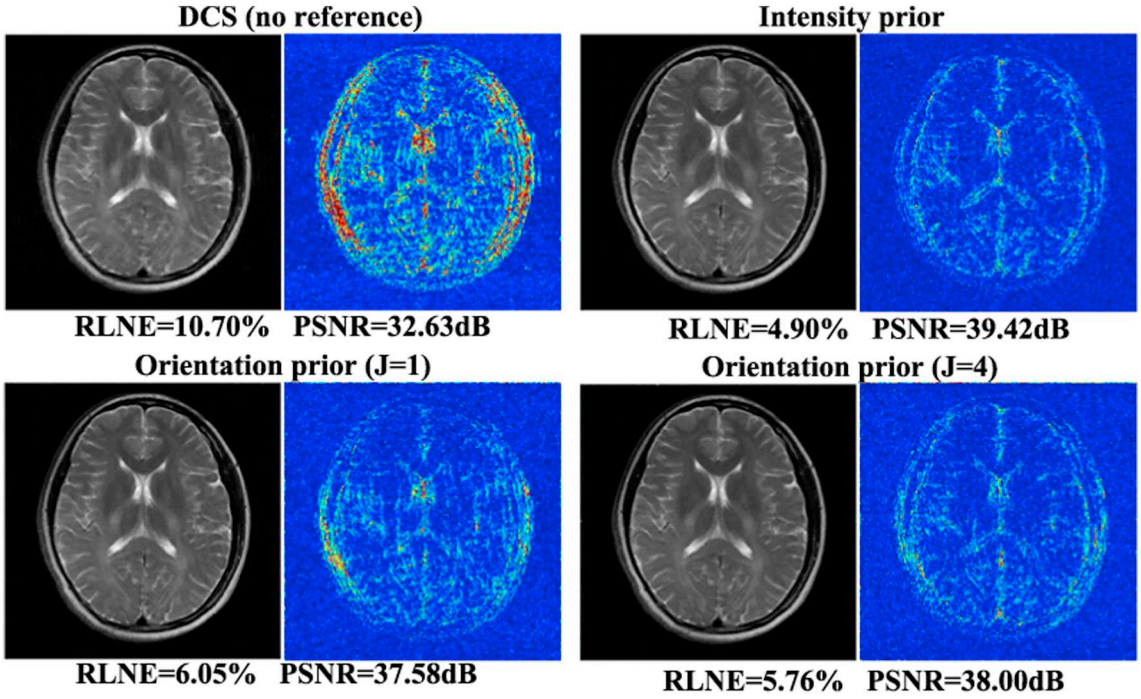

Fig. 8. The comparison of the proposed method with varying degree of similar reference guided priors for a fixed 1D undersampling mask and reduction factor of 3. The corresponding error maps are shown at the same scale.

thickness = 5.0 mm, TR = 2000/5000 ms, TE = 9.7 ms, bandwidth = 123.26 Hz/pixel). The 1D undersampling pattern with reduction factor of 4 was adopted. Since the T1-weighted image is usually acquired faster than PD and T2-weighted images, here the T1-weighted image is regarded as the reference image and T2-weighted image is regarded as the target image. Observed from the zoomed-in part in Fig. 6, the SAKE method has the worst recovery and loses much detail in reconstructed image. SparseBLIP returns results that contain some blocky artifacts. The FJTV provides a better edge shaping than the SAKE and SparseBLIP, but it still has obvious reconstruction errors especially at edge regions. As we expect, though the target and reference images have different contrasts, the edge orientation is consistent between them. Therefore, the proposed method is still able to provide an estimated image that is visually closes to the original image and has higher reconstruction accuracy in edge-preserving than other methods.

The multi-slice image dataset was scanned with a 3 T Siemens scanner using the gradient echo pulse sequence with 12-channel head coil array (matrix size = 256 × 256, FOV = 200 × 200 mm^2, slice thickness = 3.0 mm, TR = 350 ms, TE = 2.88 ms). The 1D undersampling pattern with reduction factor of 4 was conducted. The results are presented in the Fig. 7. The SAKE, SparseBLIP and FJTV methods all returned images with obvious blur and aliasing, while the proposed method consistently provided a better reconstruction than other methods, though the target and reference image have some structure mismatches. This might be because on the one hand the target and reference images share similar grey-level intensity on this dataset; on the other hand, we use multi-scale scheme to extract reference edge priors in gradient domain, which can robustly exploit the fuzzy structure information. Besides, we use a weighting scheme to control the strength of the smoothing, which avoids degradation of image quality.

4. Discussion

4.1. The advantage of the proposed reference guided regularizations

The reason why the proposed method is superior to the other methods is that it simultaneously takes advantage of the grey-level intensity and edge orientation priors extracted from the reference image on top of exploiting the joint sparsity of the target image in finite difference domain. In this subsection, we evaluate the advantage of the proposed method and its performance with varying degrees of similar priors from the reference image. The experiment is conducted on the multi-echo brain MR dataset with 1D undersampling mask and reduction factor of 3.

We can observe from the Fig. 8 that the conventional DCS method ($\lambda_2 = 0$ and $\gamma = 1$) produces an image that exhibits severe aliasing artifacts and loses lots of edge information. The other reference guided reconstructions significantly remove the artifacts and preserve the edges. Among them, the intensity prior based performance is better than that based on the edge orientation prior. This is because that the experimental images have the same contrast and intensity prior based regularization can further benefit the reconstruction. We also have compared the reconstruction quality of the proposed method with different scales based edge orientation regularizations. As shown in the error maps, the reconstruction with large scale ($J = 4$) further suppress the aliasing artifacts and provides meaningful edge structures.

4.2. Comparison with the joint NLINV method

In this subsection, we take the case into consideration that the reference image is down-sampled so as to ensure the overall acceleration of the target and reference MR images. In this part, the target image and reference images are under-sampled by reduction factor of 5 and 2 respectively. We propose to use a method similar to SparseBLIP to alternately reconstruct target and reference images. Firstly, we obtain the DCS reconstruction result of target image, then the reconstructed image is used as the reference to improve the reconstruction of original reference image from under-sampled k-space. Next the estimated reference image can be plugged to further help reconstruct the target image. Subsequently, we alternate between updating the target image and updating the reference image through iterations to obtain the good solution.

We compared with the Joint_NLINV method [32] exploited the

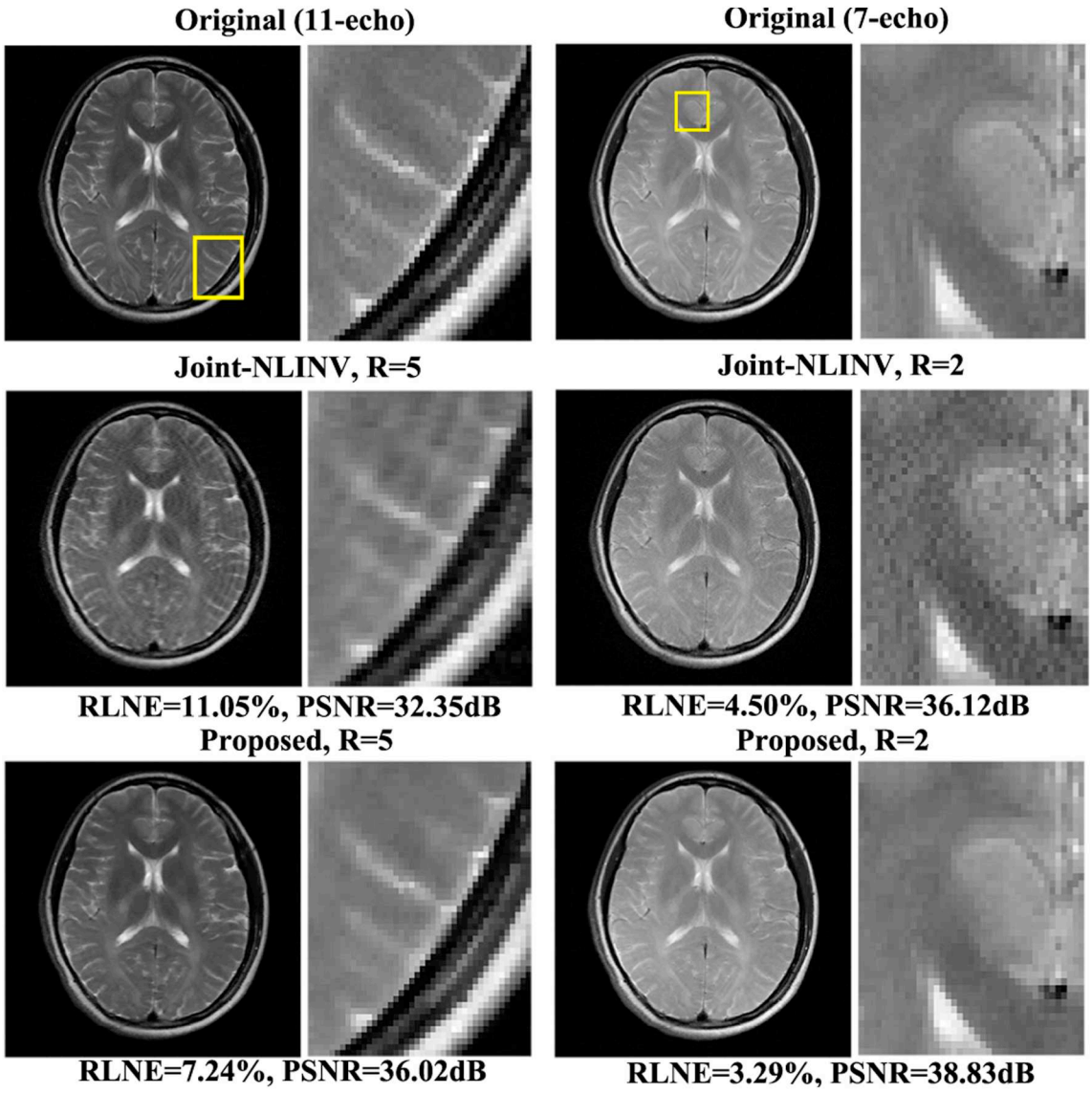

Fig. 9. The comparison of the proposed method and the Joint-NLINV method. The 7-th echo image (reference image) with 50% sampled data and the 11-th echo image (target image) with 20% sampled data. The 1D undersampling mask is used. The part enclosed by the yellow box has been enlarged for better visualization. (For interpretation of the references to colour in this figure legend, the reader is referred to the web version of this article.)

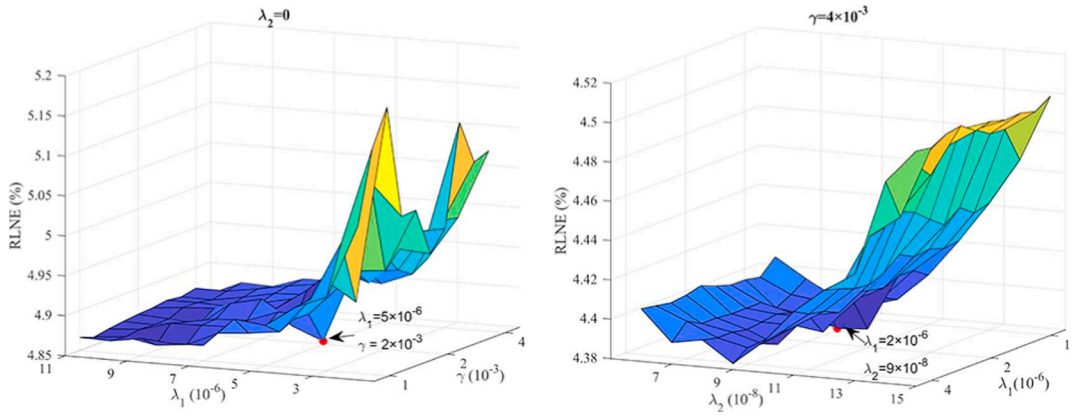

Fig. 10. Sensitivity of the proposed model to parameter selection. The experiment is conducted on in-vivo multi-echo brain image datasets. Left: the plots of RLNE versus various parameter pairs (λ_1 and γ); Right: the plots of RLNE versus various parameter pairs (λ_1 and λ_2). Each point on the surface represents an instance of parameter pairs. The desired parameter pair with best selection is marked by the red points. (For interpretation of the references to colour in this figure legend, the reader is referred to the web version of this article.)

calibrationless parallel imaging reconstruction jointly in multi-echo or contrast data, which simultaneously reconstructs coil sensitivities and image content by extending the nonlinear inversion reconstruction approach (NLINV) [9]. The specific results are shown in Fig. 9. We can observe from the zoomed-in parts that the returned images using Joint NLINV method have obvious noise and structure-like artifacts. Our proposed method can largely suppress the aliasing artifacts and effectively recover fine details in the estimated target and reference images.

4.3. Parameter selection and sensitivity

In this work, we adopt an empirical way to determine the regularization parameters of the proposed method. Specifically, they can be chosen based on the following proportional relation:

$$\lambda_1 \propto \frac{M\sigma^2}{\sum_{\alpha=1}^{2} (\gamma^* \|\mathbf{D}_\alpha \widehat{\mathbf{X}}\|_{2,1} + (1-\gamma^*)\|\mathbf{D}_\alpha(\widehat{\mathbf{X}} - \mathbf{X}_r)\|_{2,1})}$$

$$\lambda_2 \propto \frac{M\sigma^2}{\sum_{\beta=1}^{2} \|\mathbf{D}_\beta(\widehat{\mathbf{X}}, \mathbf{X}_r)\|_{2,1}}$$

where σ^2 is the estimated noise variance in k-space or the background of the target image. $\widehat{\mathbf{X}}$ is the reconstruction result of the DCS method. The parameter γ^* can be computed by the mutual information (MI) [33,34] between target and reference images. We have,

$$\gamma^* = 1 - \sum_{i,j} p(i,j)\, log\, \frac{p(i,j)}{p(i)p(j)}$$

where $p(i,j)$ denotes the joint probability distribution [34] of point-pairs in target and reference images that are considered as two random variables at each pixel location, the $p(i)$ and $p(j)$ are marginal probability distribution of target and reference images respectively. Fig. 10 represents the reconstruction results on the multi-echo brain dataset with various parameter pairs. The red point indicates the best regularization parameters with minimum RLNE values. The performance of reconstruction with only intensity priors incorporated ($\lambda_2 = 0$) is relatively sensitive to λ_1 when γ lies within the range of $[1 \times 10^{-3}, 4 \times 10^{-3}]$. In addition, we can notice that the parameter λ_2 plays a key role since the reconstruction is less sensitive to λ_1 when λ_2 and γ are fixed. The reconstructions using a large λ_2 would degrade image quality. For all tests, the λ_1 and λ_2 usually lie within the range of $[1 \times 10^{-6}, 2 \times 10^{-6}]$ and $[4 \times 10^{-8}, 1 \times 10^{-7}]$ respectively.

4.4. Limitation and further work

The quality of the reference image plays a significant role in the proposed technique. The high consistency between target and reference image can provide sufficient priors to improve the performance of joint reconstruction. In the future, we can consider the motion model and registration before the reconstruction task. Actually, for the rigid or non-rigid motion problem, some methods based on image registration techniques [35–37] can be used to correct the mismatches between the target image and reference image. However, this goes beyond the scope of this work, so those results are not fully reported here.

For the RT, the proposed method is relatively worse than other methods except the SAKE method. We can use a fast preconditioning [38,39] to efficiently accelerate the reference guided CS-PI joint reconstruction in NLCG algorithm.

5. Conclusion

Compared with the conventional methods in PI, our proposed method with the reference guided priors incorporated has superior ability of preserving fine edges and suppressing artifacts even when the reduction factor is high. In addition, the proposed reference guided priors can be applied in many other MRI fields where a reference image can be easily obtained.

Acknowledgments

The authors would like to thank the reviewers for their valuable advice on this paper. The authors also thank Zhilang Qiu for providing the in-vivo human brain MR dataset for the experiments in this article.

References

[1] Donoho DL. Compressed sensing. IEEE Trans Inf Theory 2006;52(4):1289–306.
[2] Candès EJ, Romberg J, Tao T. Robust uncertainty principles: exact signal reconstruction from highly incomplete frequency information. IEEE Trans Inf Theory 2006;52(2):489–509.
[3] Chartrand R. Exact reconstruction of sparse signals via nonconvex minimization. IEEE Signal Process Lett 2007;14(10):707–10.
[4] Pruessmann KP, Weiger M, Scheidegger MB, Boesiger P. Sense: sensitivity encoding for fast MRI. Magn Reson Med 1999;42(5):952–62.
[5] Sodickson DK, Manning WJ. Simultaneous acquisition of spatial harmonics (smash): fast imaging with radiofrequency coil arrays. Magn Reson Med 1997;38(4):591–603.
[6] Griswold MA, Jakob PM, Heidemann RM, Nittka M, Jellus V, Wang J, et al. Generalized autocalibrating partially parallel acquisitions (grappa). Magn Reson Med 2002;47(6):1202–10.
[7] Lustig M, Pauly JM. Spirit: iterative self-consistent parallel imaging reconstruction from arbitrary k-space. Magn Reson Med 2010;64(2):457–71.
[8] Uecker M, Lai P, Murphy MJ, Virtue P, Elad M, Pauly JM, et al. Espirit–an eigenvalue approach to autocalibrating parallel MRI: where sense meets grappa. Magn Reson Med 2014;71(3):990–1001.
[9] Uecker M, Hohage T, Block KT, Frahm J. Image reconstruction by regularized nonlinear inversion–joint estimation of coil sensitivities and image content. Magn Reson Med 2008;60(3):674–82.
[10] Liu B, Zou YM, Ying L. Sparsesense: application of compressed sensing in parallel MRI. International conference on information technology and applications in biomedicine. 2008. p. 127–30.
[11] Liang D, Liu B, Wang J, Ying L. Accelerating SENSE using compressed sensing. Magn Reson Med 2009;62(6):1574–84.
[12] Chaari L, Pesquet JC, Benazza-Benyahia A, Ciuciu P. A wavelet-based regularized reconstruction algorithm for sense parallel MRI with applications to neuroimaging. Med Image Anal 2011;15(2):185–201.
[13] Liang D, Wang H, Chang Y, Ying L. Sensitivity encoding reconstruction with nonlocal total variation regularization. Magn Reson Med 2011;65(5):1384–92.
[14] Chen Y, Hager W, Huang F, Phan D, Ye X, Yin W. Fast algorithms for image reconstruction with application to partially parallel MR imaging. SIAM J Imag Sci 2012;5(1):90–118.
[15] Otazo R, Li F, Chandarana H, Block T, Axel L, Sodickson DK. Combination of compressed sensing and parallel imaging for highly-accelerated dynamic MRI. IEEE international symposium on biomedical imaging. 2012. p. 980–3.
[16] Shin PJ, Larson PE, Ohliger MA, Elad M, Pauly JM, Vi-gneron DB, et al. Calibrationless parallel imaging reconstruction based on structured low-rank matrix completion. Magn Reson Med 2014;72(4):959–70.
[17] Trzasko JD, Manduca A. Clear: calibration-free parallel imaging using locally low-rank encouraging reconstruction. The proc. 20th annual meeting of ISMRM. 2012. p. 517.
[18] Majumdar A, Ward RK. Calibration-less multi-coil mr image reconstruction. Magn Reson Imaging 2012;30(7):1032.
[19] Majumdar A, Chaudhury KN, Ward R. Calibrationless parallel magnetic resonance imaging: a joint sparsity model. Sensors 2013;13(12):16714.
[20] Ying L, Sheng J. Joint image reconstruction and sensitivity estimation in sense (jsense). Magn Reson Med 2010;57(6):1196–202.
[21] She H, Chen RR, Liang D, Dibella EV, Ying L. Sparse blip: blind iterative parallel imaging reconstruction using compressed sensing. Magn Reson Med 2014;71(2):645–60.
[22] Chun IY, Adcock B, Talavage T. Efficient compressed sensing sense pMRI reconstruction with joint sparsity promotion. IEEE Trans Med Imaging 2015;35(1):354–68.
[23] Beck A, Teboulle M. Fast gradient-based algorithms for constrained total variation image denoising and deblurring problems. IEEE Trans Image Process 2009;18(11):2419–34.
[24] Beck A, Teboulle M. A fast iterative shrinkage-thresholding algorithm for linear inverse problems. SIAM J Imag Sci 2009;2(1):183–202.
[25] Chen C, Li Y, Huang J. Calibrationless parallel MRI with joint total variation regularization. International conference on medical image computing and computer-assisted intervention. 2013. p. 106–14.
[26] Lustig M, Donoho D, Pauly JM. Sparse MRI: the application of compressed sensing for rapid MR imaging. Magn Reson Med 2007;58(6):1182–95.
[27] Peng X, Zhu Q, Wang S, Liang D. Reference guided CS-MRI with gradient orientation priors. IEEE international conference of the engineering in medicine and biology society (EMBC). 2015. p. 7498–501.
[28] Peng X, Wang S, Zhu Q, Liang D. Reference-guided CS-MRI with gradient

orientation priors. The proc. 24th annual meeting of ISMRM. 2016. p. 4232.
[29] Liu P, Huang F, Li G, Liu Z. Remote-sensing image denoising using partial differential equations and auxiliary images as priors. IEEE Geosci Remote Sens Lett 2012;9(3):358–62.
[30] Wang LZ, Lu K, Liu P. Compressed sensing of a remote sensing image based on the priors of the reference image. IEEE Geosci Remote Sens Lett 2015;12(4):736–40.
[31] Chen L, Guo L, Gao SW. Edge extraction method with multi-scale gradient. J Comput Appl 2008;28(12):3129–31.
[32] Bilgic B, Zhao B, Chatnuntawech I, Wald L, Setsompop K. Calibrationless parallel imaging in multi echo/contrast data. The proc. 25th annual meeting of ISMRM. 2017. p. 0139.
[33] Guo W, Huang F. A local mutual information guided denoising technique and its application to self-calibrated partially parallel imaging. Med Image Comput Comput Assist Interv 2008;11(2):939–47.
[34] Wells WM, Viola P, Atsumi S, Nakajima Hand, Kikinis R. Multi-modal volume registration by maximization of mutual information. Med Image Anal 1996;1(1):35–51.
[35] Du H, Lam F. Compressed sensing MR image reconstruction using a motion-compensated reference. Magn Reson Imaging 2012;30(7):954–63.
[36] Mun S, Fowler JE. Motion-compensated compressed-sensing reconstruction for dynamic MRI. IEEE international conference on image processing (ICIP). 2013. p. 1006–10.
[37] Filipovic M, Vuissoz PA, Codreanu A, Claudon M, Felblinger J. Motion compensated generalized reconstruction for free-breathing dynamic contrast-enhanced MRI. Magn Reson Med 2011;65(3):812–22.
[38] Xu Z, Li Y, Axel L, Huang J. Efficient preconditioning in joint total variation regularized parallel MRI reconstruction. International conference on medical image computing and computer-assisted intervention. 2015. p. 563–70.
[39] Li R, Li Y, Fang R, Zhang S, Pan H, Huang J. Fast preconditioning for accelerated multi-contrast MRI reconstruction. International conference on medical image computing and computer-assisted intervention. 2015. p. 700–7.